Joule

CellPress
OPEN ACCESS

Perspective

Photonics roadmap for ultra-high-temperature thermophotovoltaics

Mariama Rebello Sousa Dias,[1,2] Tao Gong,[2,4] Margaret A. Duncan,[2] Stuart C. Ness,[3] Scott J. McCormack,[2] Marina S. Leite,[2,*] and Jeremy N. Munday[4,*]

SUMMARY

The ability to control thermal emission is crucial for the thermal regulation of devices, barrier coatings, and thermophotovoltaic (TPV) systems. However, only a limited number of naturally occurring materials are stable at high temperatures (>1,800°C), and their emission spectra are set *a priori* by their intrinsic optical properties. Optical structures involving nanoscale textures can result in tunable emission spectra, albeit stable only at much lower temperatures. Here, we present an alternative approach that enables temperatures beyond 1,800°C through a bilayer stack achieved by combining the optical and thermal properties of 2,809 coating/substrate pairs. By varying the film thickness, we tailor the emission spectrum to create high-temperature, stable emitters. We illustrate this effect in combination with the most common TPV systems (GaSb, Ge, InGaAs, and InGaAsSb), showing power conversion efficiencies approaching 50% and power outputs as high as 10.2 W cm^{-2}. These concepts can be expanded to other high-temperature photonic applications for the spectral control of thermal emission.

INTRODUCTION

The concept of thermophotovoltaics (TPVs) relies on the use of a power source to heat an optical emitter, which, in turn, selectively emits optical (and/or thermal) radiation toward a conventional photovoltaic (PV) cell (see Figure 1A).[1] A primary feature of TPV systems is their flexibility regarding the power source that heats the emitter, which could be solar, chemical, nuclear, etc. This versatility could enable TPV to be applied in a plethora of situations, including direct thermal-to-electrical power, waste heat recovery, and an alternative to thermal storage, among others.

Although TPV has the potential to be a scalable technology, ultra-high temperature (>1,800°C) is desired for effective conversion of thermal radiation to, ultimately, electrical power because higher temperatures result in increased photon flux from the emitter (which is also accompanied by a shift in its maximum to shorter wavelengths and better alignment with the band gap of high-quality PV cells). For instance, an increase in temperature from 1,200°C to 1,800°C has been attributed to an absolute efficiency enhancement of nearly 10%.[2] Nevertheless, there is a caveat: the overall performance increase with high temperatures is primarily due to an increase in the short-circuit current density (J_{sc}) of the PV cells, yielding a higher V_{oc}; however, at very high current densities, a reduction in fill factor (FF) (caused by a rise in series resistance) diminishes these gains. Thus, the PV cell becomes current-limited beyond a certain temperature of the TPV system, which is device-dependent. Because of the abovementioned trade-off and the fact that few optical materials are

CONTEXT & SCALE

In this perspective, we present a new approach to ultra-high temperature thermophotovoltaics (TPVs), which involves bilayer structures that combine the optical and thermal properties of nearly 3,000 coating/substrate pairs. The method results in high-temperature (>1,800°C) stable emitters with spectra that are tuned to the photovoltaic cell's spectral response. The finding presents a novel pathway for designing photonic structures that can operate at ultra-high temperatures and could enable the next generation of record-efficiency lab-scale TPV systems while simultaneously paving the way for their commercialization due to the reduced complexity of the structures. Moreover, we identify several new systems for exploration with the potential for TPV efficiencies greater than 50%, involving materials with promising but unknown thermochemical stability. These structures also have the potential to be extended to other high-temperature photonic applications, including thermal regulation of devices and barrier coatings.

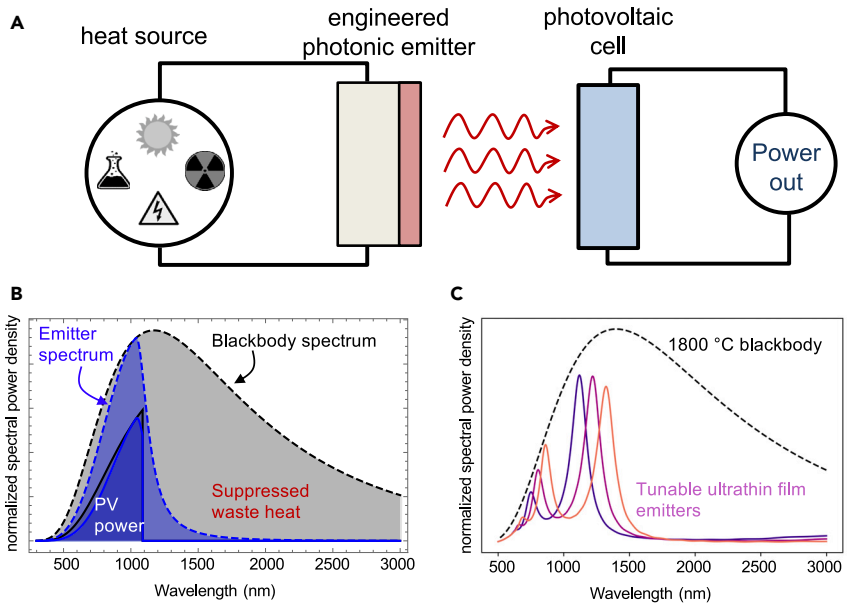

Figure 1. Concept of ultra-thin films for thermophotovoltaics

(A) Schematic of thermophotovoltaic system.

(B) Illustration of spectral power density for a blackbody spectrum (black dashed line), emitter spectrum (blue dashed line), and photovoltaic (PV) power output (solid blue line). The gray region highlights the suppressed waste heat.

(C) Normalized spectral power density as a function of wavelength for thin-film emitters with variable thickness (colored solid lines) and for a (2,073.15 K) blackbody at 1,800°C (black-dashed line).

thermochemically stable at ultra-high temperatures, we chose to focus on the photonic and thermodynamic properties of emitters that would operate at 1,800°C, as discussed later. To date, single-junction TPV devices have reached power conversion efficiencies as high as 38.8% with emitter temperatures up to 1,900°C (2,123.15 K).[2–5] Note: a recent demonstration of a combined multijunction/TPV configuration has reached 40% efficiency.[6] To improve their power conversion efficiency, the critical design objective was to minimize energy losses between the hot emitter, which must operate at high temperatures (>1,000°C or 1,273.15 K), and the PV cell.

One promising pathway to mitigate losses is using ultra-high-temperature photonics to design structures to emit a radiation spectrum that is tuned to the PV cell's spectral response[7] (Figure 1A). Demonstrated TPV conversion efficiencies have increased significantly in the past few years due to the spectral control between the emitter and the cell using architectures ranging from incorporating high-quality optical back reflectors[2–6] to photonic crystals,[8,9] spectral optical filters,[4] and metamaterials.[10–12] These distinct designs have a common aspect: they all rely on photonic structures that must operate at high temperatures.

In the realm of TPV, when working with a given PV cell (with a band-gap energy E_g), a good thermal emitter should preferentially emit in-band photons ($\hbar\omega \geq E_g$) and simultaneously suppress out-of-band photons ($\hbar\omega < E_g$). Moreover, parasitic absorption of these out-of-band photons within the cell would result in waste heat.[13–16] Hence, a black body emitter with unity emissivity does not meet the criteria because its radiation includes a significant portion of out-of-band photon energies (black-dashed line in

[1]Department of Physics, University of Richmond, Richmond, VA 23220, USA

[2]Department of Materials Science and Engineering, University of California, Davis, Davis, CA 95616, USA

[3]Department of Chemical Engineering, University of California, Davis, Davis, CA 95616, USA

[4]Department of Electrical and Computer Engineering, University of California, Davis, Davis, CA 95616, USA

*Correspondence: mleite@ucdavis.edu (M.S.L.), jnmunday@ucdavis.edu (J.N.M.)

https://doi.org/10.1016/j.joule.2023.08.015

Figure 1B). Therefore, the emissivity profile of an effective emitter must be carefully tailored to yield the aforementioned emission spectrum (blue-dashed line in Figure 1B). Simultaneously, only a fraction of the absorbed in-band photon energy can be converted into electrical power (solid-black line in Figure 1B) due to thermalization, free-carrier absorption, and the limited diffusion length in a practical PV cell.[4,17,18] Narrow-banded emission right above the band-gap energy is favored to mitigate thermalization, albeit at the cost of reduced output power density.[14,18] To achieve the desired emission at extreme temperatures and/or the harsh environments relevant to many real-world applications (e.g., TPV), emitter design concepts involving metamaterials encompassing nano-structuring in 2D or 3D arrays of refractory metals (e.g., Ta and W) and transition metal oxides or nitrides (e.g., TiN and HfO_2)[19–23] suffer from longevity robustness. Alternatively, we suggest a simpler but mechanically more robust structure consisting of a thin-film layer on a substrate (Figure 1C), which has the potential to overcome this challenge because the thickness of the coating layer can tailor the narrow peak emission to match the band-gap energy of the PV cell. The emission peak is attributed to both intrinsic material absorption and interference effects inside the absorbing thin-film layer (note: this peak depends upon the optical phase accumulation within the layer and at the boundaries, material dispersion, and intrinsic material resonances). For practical consideration as a thermal emitter, both the thin film and the substrate materials must endure ultra-high temperatures, >1,800°C (2,073.15 K), a temperature range unsuitable for noble metals and conventional semiconductors, suggesting the need for screening alternative materials, beyond the commonly used options.

Here, we present a new paradigm for TPV using emitters consisting of a single, thin film atop a substrate that can surpass the state-of-the-art efficiency and function at ultra-high temperatures (>1,800°C or 2,073.15 K). For the five systems described in this perspective, we have chosen an emitter temperature of 1,800°C. For example, we show the potential for a single-junction GaSb-TPV device to produce power conversion efficiency >49% using a two-layer emitter structure that is predicted to be thermochemically stable at 1,800°C. We also find trade-offs between efficiency and power density depending upon the chosen emitter material combination (when listing combinations, we use the convention: [coating]/[substrate]). For example, we find that a single-junction silicon (Si) TPV system with a BN/AlN emitter can lead to 51.5% efficiency, albeit at a low power density of 0.29 W cm^{-2} (a more practical combination would be an AlN/Mo emitter, which can achieve an efficiency of 33.3% at a power density of 1.78 W cm^{-2}). To achieve these results, we provide and utilize a library of refractive indices ($\tilde{n} = n + ik$) for 53 materials with melting points above 2,000°C (2,273.15 K). The thermal stability of the emitters is also assessed, through the coefficient of thermal expansion mismatch between the two layers, their thermochemical stability, via phase equilibria, and their vapor pressure. By evaluating the available data of both optical and thermal properties of 2,809 coating/substrate pairs, we expand our analyses and downselect the most promising emitter options for five typical TPV cell types: Si, germanium (Ge), GaSb, indium gallium arsenide (InGaAs), and indium gallium arsenide antimonide (InGaAsSb). We find a power conversion efficiency of >45% for all systems at 1,800°C (2,073.15 K), with a maximum power density of up to 10 W cm^{-2}. For higher temperatures, the emitter spectrum will shift to shorter wavelengths, allowing a better alignment with the TPV band gap for many cell types. Overall, our approach avoids the scalability challenges associated with nanofabrication (e.g., large-scale nanolithography) using, instead, thin-film coating techniques (e.g., sputtering, sol-gel processes, etc.), which could enable TPV production at scale. Moreover, the optical and thermal data provided here could be used for the inverse design of complex photonic structures for any application that requires spectral management, such as thermal barrier

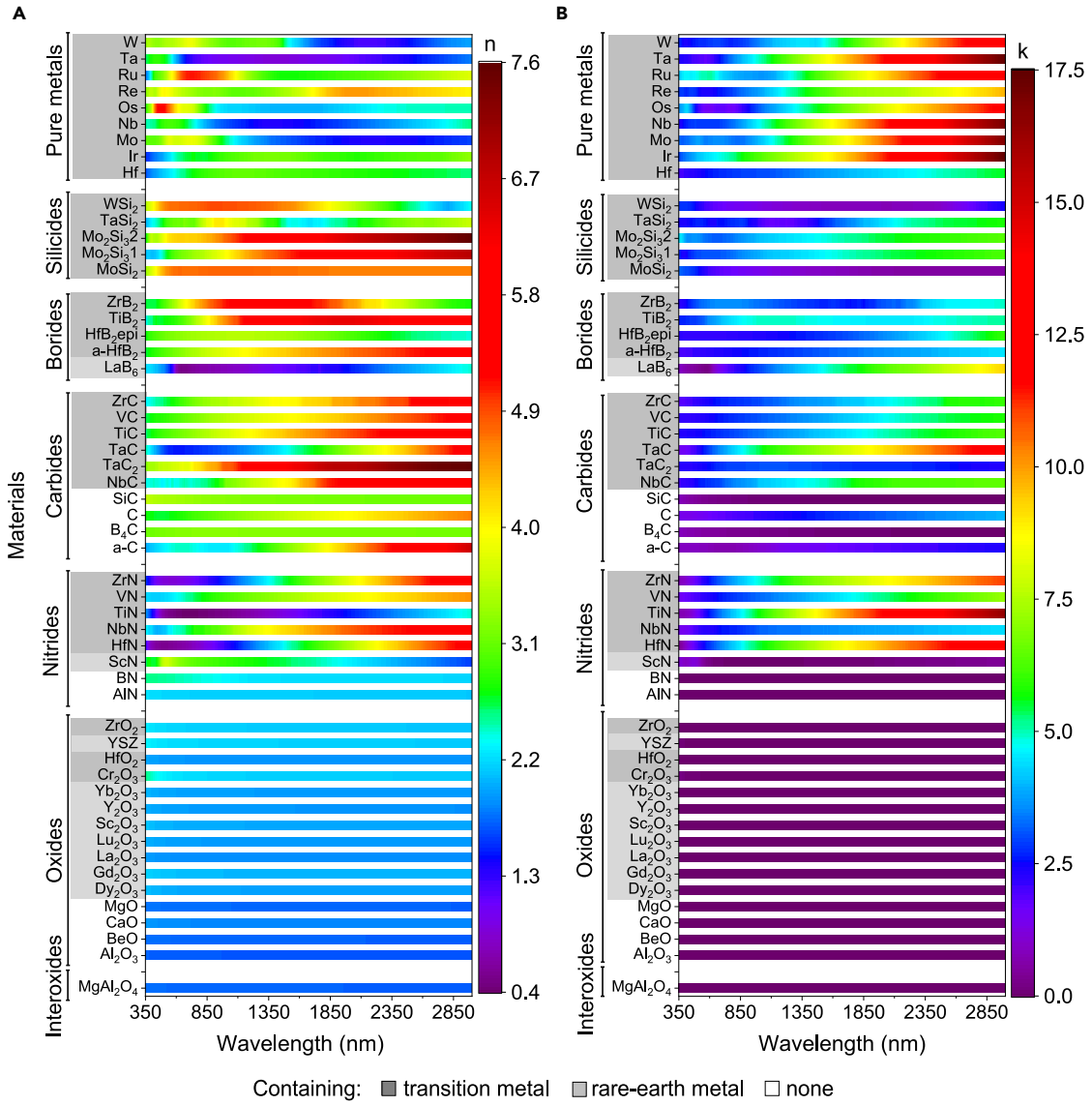

Figure 2. Refractive index library for materials with melting point >2,000°C (2,273.15 K)

(A) Real (*n*) and (B) imaginary (*k*) parts of the refractive index for materials with melting point >2,000°C (2,273.15 K). The data presented have been acquired from Palik,[24] Antonov et al.,[25] Tanaka et al.,[26] Hernández-Pinilla et al.,[27] Hoat,[28] Yang et al.,[29] Heide et al.,[30] Modine et al.,[31,32] Jubair et al.,[33] Koide et al.,[34] Larruquert et al.,[35,36] Guo et al.,[37] Banerjee et al.,[38] Saha et al.,[39] Adachi,[40] and Pastrňák and Roskovcová[41] and measured by ellipsometry.

coatings, heat waste recovery, and other high-temperature photonic devices, mitigating the weariness of conventional Edisonian methods.

RESULTS AND DISCUSSION

Ultra-high-temperature optical materials

To engineer the optical behavior of an emitter structure, the dielectric response of the individual constituents is needed. Thus, we have compiled the complex refractive indices ($\tilde{n} = n + ik$) of 53 of the top 100 highest melting point materials (Figure 2). Here, we opt to group the data by material classification, which facilitates the comparison of similar features within the same material category. Specifically, Figure 2 shows the real (*n*) and imaginary (*k*) parts of $\tilde{n}$ within the spectral range of 350–3,000 nm for nine pure metals,[24] five silicides,[25–27] five borides,[28–30] ten

carbides,[24,31–36] eight nitrides,[24,37–41] fifteen oxides,[24,42–48] and one interoxide. Hafnium (Hf), yttria-stabilized zirconia (YSZ), and the spinel $MgAl_2O_4$ bulk samples are characterized via spectroscopic ellipsometry. Note that the optical data have been carefully interpolated and extrapolated in situations where the information available in the literature is smaller than the spectral range (see Figures S1–S7 for extended models of the refractive index).

As a general design goal, we desire narrowband emission peaked near the band gap of the proposed TPV device. However, the optical response of the bilayer emitter results from a complex interplay between the dispersive dielectric properties of both the substrate and the coating, as well as the coating thickness, *d*. With a reflective, metallic substrate, we focus on the properties of the coating that result in such a spectrum. In general, materials that have regions of significant dispersion (e.g., arising from an optical resonance within the material) near the wavelength of interest result in a narrow emission peak at that wavelength. The film thickness can be used to further enhance the resonance by choosing *d* to create a cavity mode matched to the material's absorption resonance. For a material whose intrinsic resonance is far from the TPV band gap of interest, a narrow bandwidth emission can still be achieved by only using the cavity mode. However, thicker coatings are generally necessary, which may result in the generation of additional IR (infrared) resonances that could increase out-of-band thermal emission; hence, care must be taken to avoid decreasing the TPV efficiency when thicker films are used.

Refractory metals are generally good candidates for TPV emitters because they are thermally stable at ultra-high temperatures in inert atmospheres.[11,49,50] For GaSb-TPV systems, W provides some spectral selectivity due to its wavelength dependence of the refractive index, which is why it is a common emitter in TPV applications. At room temperature, the band-edge of its intraband transition, characterized by a sharp decrease in the value of *n* (Figure 2A), is located near the band gap of the GaSb cell. Thus, its spectral characteristics have an absorption/emission peak close to the band gap of the PV cell, diminishing at lower energies (Figure 2B). The dependence of $\tilde{n}$ with temperature of W is almost invariant in the visible region of the electromagnetic spectrum and slight changes in the infrared region due to a decrease in the plasma frequency of the Drude term describing the intraband transition contribution.[51] For these reasons (and noting that materials are chosen that will not undergo a phase change under the conditions considered here), the room temperature values are used. In general, the material's optical properties depend on the class of the material, fabrication conditions, electromagnetic wave frequency, and temperature variation range of consideration.[52–56] If materials that undergo significant optical property changes at higher temperatures are chosen, a re-optimization of the emitter structure may be necessary. If the changes predominantly occur beyond the band gap of the PV cell, their effect on the cell's power will be minimal but can affect the overall TPV efficiency (increasing or decreasing it). To avoid adversely affecting the efficiency, a back reflector can be included so that sub-band-gap photons are returned to the emitter.

TPV performance with dual-layer emitters

The power conversion efficiency of TPV systems is directly dependent on how efficiently heat is converted to electricity. To this end, one must suppress losses such as absorption and emission of low-energy photons, thermalization of high-energy carriers within the cell, non-radiative electron-hole pair recombination, Ohmic losses, and parasitic heat losses to the environment. To evaluate the performance of TPV systems using emitters composed of the materials listed in Figure 2, we define a

figure-of-merit (FOM) that represents the heat-input-to-power-output efficiency for an idealized TPV system as:

$$\mathrm{FOM} = \frac{P_{\mathrm{cell}}}{P_{\mathrm{emit}}}, \qquad \text{(Equation 1)}$$

where P_{cell} is the maximum electrical power generated by the cell, and P_{emit} is the incident power generated by the emitter. Here, $P_{\mathrm{cell}} = V_{\mathrm{OC}} J_{\mathrm{SC}} FF$, where V_{OC} is the open-circuit voltage, J_{SC} is the short-circuit current density, and FF is the fill factor of the PV cell. Also, our calculations are performed within the limit of the optical data available (350–3,000 nm). The electrical power generated under illumination is obtained directly from the cell current density-voltage (J-V) characteristics given by Bermel et al.,[57] Almora et al.,[58] and Rau[59]:

$$\begin{aligned} J &= \int_{350}^{3,000} \left[q\epsilon(\lambda)\,\overline{n}_{\mathrm{B}}(\lambda, T) IQE\right] d\lambda - \left[e^{\frac{qV}{k_b T_c}} - 1\right] \int_{350}^{3,000} \left[q\,\overline{n}_{\mathrm{B}}(\lambda, T_c) IQE\right] d\lambda \\ &= J_{\mathrm{L}} - J_0 \left[e^{\frac{qV}{k_b T_c}} - 1\right] \end{aligned} \qquad \text{(Equation 2)}$$

where J_{L} is the light-generated current density, J_0 is the dark current density, q is the charge of the electron, k_b is the Boltzmann constant, T_c is the temperature of the PV cell, $\epsilon(\lambda)$ is the emissivity spectrum of the emitter, $\overline{n}_{\mathrm{B}}(\lambda, T)$ is the blackbody photon density spectrum, and IQE is the internal quantum efficiency of the PV cell. To be agnostic to the individual cell technologies, we assume ideal antireflection coatings and that the IQE is a Heaviside step function (=1 above the band gap) in the following calculations. Note that the model does not include additional terms for series or shunt resistance or forms of non-radiative recombination, as they will be design and fabrication-specific. The incident power is calculated from the spectral emissivity of the emitter; thus:

$$P_{\mathrm{emit}} = \int_{350}^{3,000} \epsilon(\lambda) B(\lambda, T) d\lambda \qquad \text{(Equation 3)}$$

where $B(\lambda, T)$ is the blackbody power spectrum (Figure S8).

Ideally, an optical emitter should have high optical performance, long-term high-temperature stability, an ease of integration within a TPV system, be scalable, and have low costs.[14] Considering all these constraints, we exploit a dual-layer design composed of a thin-film coating and a substrate to finely tune the absorption/emission spectrum of the emitter. Selective thermal emitters are designed to suppress out-of-band emission and emit in-band radiation. The coating/substrate configuration offers significant benefits regarding the fabrication of planar, omnidirectional, and polarization-insensitive structures.[60] Thus, we optimize the thickness of the coating layer of 2,809 coating/substrate pairs (Figure S9) to achieve the highest FOM for each TPV system with the emitter operating at 1,800°C (2,073.15 K). At other temperatures, the emitter should be reoptimized to achieve maximum FOM. The top-performing emitter material combinations remain similar, but the coating thicknesses change slightly (i.e., the coating thickness to optimize the FOM generally shifts to smaller thicknesses as the temperature is increased).

Figure 3A displays the FOM of the thickness-optimized pairwise combination of coating-substrate layers for the emitter of a GaSb-TPV system. Our calculations show that FOMs >50% are feasible for SiC/W and AlN/Mo emitters, and many other combinations approach 50%. Refractory metals as substrates combined with oxide

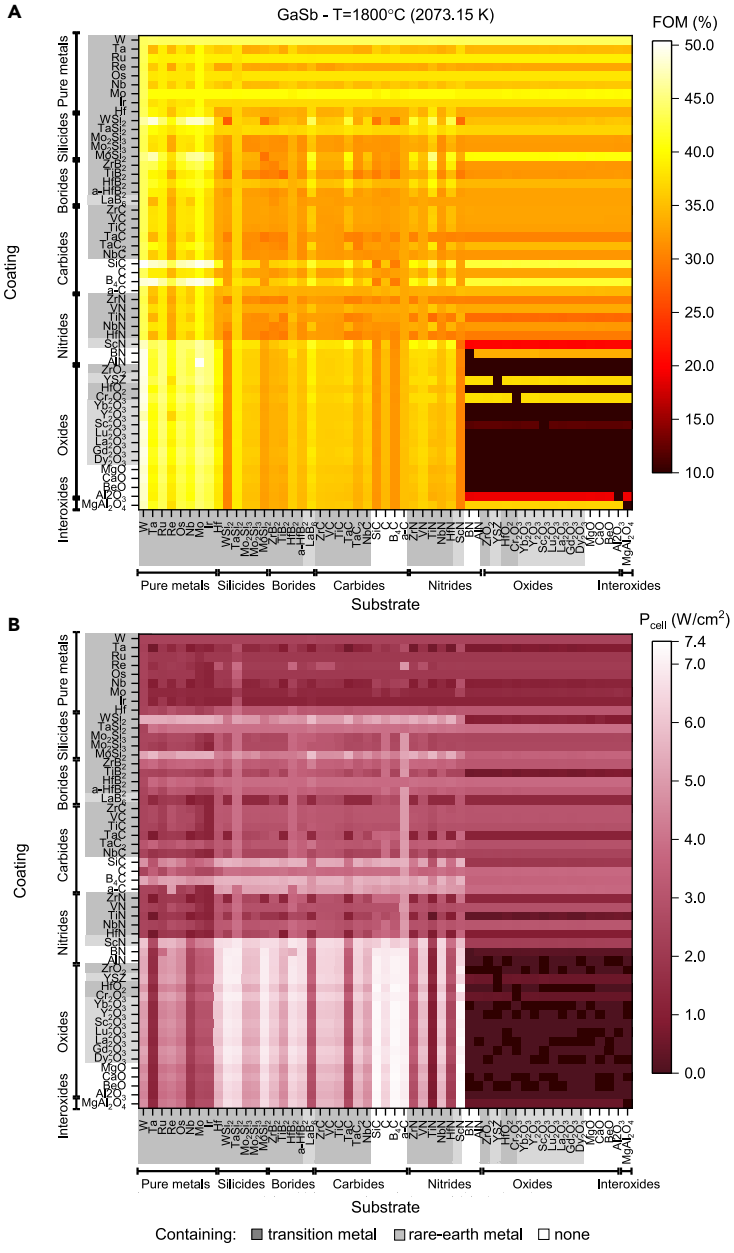
A
GaSb - T=1800°C (2073.15 K)
FOM (%)
50.0
45.0
40.0
35.0
30.0
25.0
20.0
15.0
10.0
Coating
Pure metals
Silicides
Borides
Carbides
Nitrides
Oxides
Interoxides
Substrate
B
P_cell (W/cm²)
7.4
7.0
6.0
5.0
4.0
3.0
2.0
1.0
0.0
Containing: transition metal rare-earth metal none
C
FOM (%)
45
30
15
0
0
1
2
3
4
5
6
7
P_cell (W/cm²)

Figure 3. Surpassing the state-of-the-art for thermophotovoltaics

(A) Heatmap associated with the figure-of-merit (FOM) of GaSb thermophotovoltaic scheme formed by thin film emitter at 1,800°C (2,073.15 K) operating temperature and GaSb photovoltaic device.

(B) Heatmap of the power generated by the GaSb cell (P_{cell}).

(C) FOM as a function of P_{cell} for all material combinations considered in (A) and (B).

or carbide coatings are promising options for emitters in this specific system (see Figure 3A). This result is a consequence of the refractive index contrast between the two layers and the optimized thickness of the coating, which leads to an enhancement of the emission of light over the appropriate spectral range. Note that adding a coating material boosts the FOM by 16.0% and 15.4% (absolute) for pure Ta and W, respectively. Conversely, most combinations only involving oxides present the lowest FOM. Because the emitter structure that generates the maximum power conversion efficiency for the TPV system is not necessarily the same one that yields the maximum output power of the cell (P_{cell}, in W cm^{-2}), we also analyze P_{cell}, as presented in Figure 3B. Here, the highest values achieved (>7.0 W cm^{-2}) encompass carbides and nitrides coated by oxides and silicides coated by oxides and nitrides. Note that the emitters using pure metals as substrates (left side of graphs presented in Figures 3A and 3B) have modest values of P_{cell}. GaSb is considered a top PV choice for TPV applications due to its low band-gap energy (E_g), its excellent quantum efficiency (>90%), especially at IR wavelengths,[61] and the cell performance being less affected at higher operating temperatures.[62] Overall, this quantitative analysis is helpful as it can guide the choice of materials depending on the application in mind. For example, in some situations with relatively high FOMs, there is a trade-off with output power (e.g., P_{cell} < 0.5 W cm^{-2}), as shown in Figure 3B. The reason for this constraint is that FOM and P_{cell} are optimized differently. P_{cell} can be improved by increasing the number of above-band-gap photons generated by the emitter without concern for their particular energy or the number of below-band-gap photons also being emitted. Alternatively, the FOM decreases when the emitted photons are not optimally used (e.g., any photons with energy significantly above the band gap do not produce any more power than band-gap energy photons, and sub-band-gap photons do not generate power at all). Figure 3C depicts the FOM as a function of P_{cell} for all emitter combinations to explicitly demonstrate this trade-off. The data clearly show that the maximum power and maximum FOM occur for different coating-substrate pairs. Through the optimization, we find many coating-substrate combinations that result in a high FOM; however, there is a large spread in output power within a given FOM range. It is also clear that there are many high-power options, although we did not optimize for output power.

In TPV, the PV cell is the component that dictates the overall design of the system. For instance, it determines which emitter configuration will result in the highest FOM value at a given temperature. Therefore, we extend our calculations to four other common TPV cell types, namely InGaAsSb, InGaAs, Ge, and Si (Figure 4). For materials that have tunable band gaps, we have chosen commonly reported values from experimentally realized TPV cells. These values also provide a wide range of band gaps. Figure 4A shows the FOM heatmap of an InGaAsSb (E_g = 0.53 eV) PV cell. We identify several material combinations with FOM values >47%, including coating layers of WSi_2, $MoSi_2$, and B_4C. Also, due to its narrow band gap, which allows for maximum harvesting of infrared radiation, P_{cell} values above 10.0 W cm^{-2} are obtained (Figure S10). For an InGaAs (E_g = 0.6 eV) cell, we again find FOMs >47% (using emitters containing SiC, WSi_2, and AlN coatings on W and Mo substrates), with other possible material combinations having P_{cell} > 9.0 W cm^{-2}

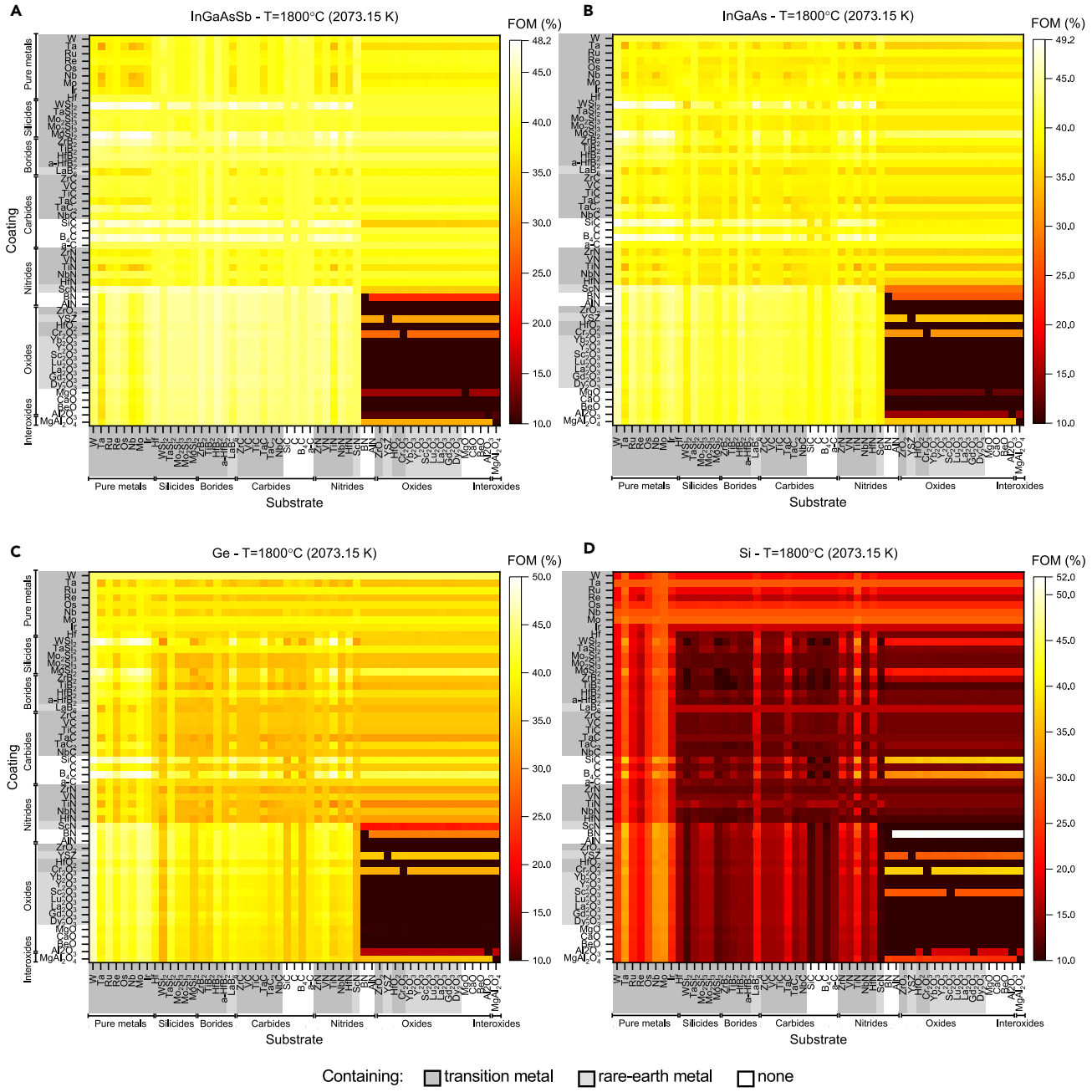

Figure 4. TPV performance

Heatmaps of figures-of-merit (FOMs) for TPV operating at 1,800°C (2,073.15 K) with (A) InGaAsSb, (B) InGaAs, (C) Ge, and (D) Si photovoltaic cells.

(see Figures 4B and S11). Figures 4C and 4D show that indirect band-gap PV cells, Ge (E_g = 0.67 eV) and Si (E_g = 1.1 eV), can achieve an FOM > 50%; however, their power densities are more modest, reaching P_{cell} = 4.2 W cm^{-2} for the Ge-TPV system (Figure S12) and <0.3 W cm^{-2} for Si-TPV (Figure S13). Specifically, using BN as a coating could provide outstanding performance (52%) when combined with oxides and interoxidics, as shown in Figure 4D. This feature is a direct consequence of the nearly constant value of n (Figure 2A), added to the wavelength-independent, dielectric behavior of the coating materials ($k \cong 0$, see Figure 2B).

Thermal stability

This section highlights the need to assess three thermal-related properties of materials to ensure the emitter's survivability: thermal expansion, thermochemical stability, and vapor pressure. As expected, depending on the experimental conditions of the TPV system, i.e., temperature and environment of operation, these parameters might differ significantly. Thus, it is important to analyze how they each influence the TPV system.

Figure 5A shows the length percent expansion (dL/L) of polycrystalline material candidates for substrates and coatings using 25°C (298.15 K) as reference. A system that may be thermochemically stable may still fail from thermomechanical constraints due to a mismatching of properties between the layered materials. The crack energy release rate (G) that drives interfacial delamination of a bilayer under plain strain and equi-biaxial pre-cracking conditions is given by $G = \frac{1+\nu}{16(1-\nu)} Ed[\Delta\alpha\Delta T]^2$, where ν is the Poisson ratio, E is the Youngs modulus, d is the thickness of the coating layer, $\Delta\alpha$ is the difference in the thermal expansion (thermal expansion mismatch) between the coating layer and the substrate, and ΔT is the change in temperature during cooling from a stress-free temperature. Delamination occurs if the crack energy release rate becomes larger than a critical value ($G > G_c$).[67,68] Thus, a top coating is less likely to delaminate during thermal cycling if G is minimized. One can achieve this condition by minimizing E or d of the coating, but it will have the most significant effect by minimizing the thermal expansion mismatch as $G \propto \Delta\alpha^2$. From Figure 5B (upper triangular), material combinations with low thermal expansion mismatches are highlighted in white (see Figure S14 for additional temperatures). A few examples of low thermal expansion mismatch combinations include the following: ZrC/LaB_6, TiN/ZrO_2, WSi_2/Mo, etc.

Phase equilibria define whether the combined solid materials can co-exist until melting without forming a (1) solid solution or an (2) intermediate compound. Figure 5B presents the materials that, when sharing an interface, are either stable or unstable, forming either (1) or (2), below their melting temperature. We obtain Figure 5B by examining a series of phase diagrams from FactSage (using SpMCBN, FTOxCN, FactPS, and Ftoxid databases)[65] and the NIST Standard Reference Database 31 (also known as the American Ceramic Society [ACerS] Phase Diagram 4.9 database),[66] all of which are available in the supplemental information (note that interfacial and surface energy effects on stability are not considered in these databases). Combinations marked as stable are those in which a zero chemical potential gradient can be achieved across the interface ($\nabla\mu = 0$) between materials with fine chemical tuning and controlled atmosphere (inert in some cases and with controlled oxygen in other cases). Due to the small solubility range of most systems that increases with temperature (defined by the solvus), one must take the latter into consideration to ensure that $\nabla\mu$ across the interface remains zero. Also, non-stochiometric systems (e.g., transition metal carbides) with phase diagrams showing a remnant phase with phase fractions below 10^{-4} are considered stable because the remnant phase can be removed by fine chemical tuning and controlled atmosphere. The stable combinations (white in Figure 5B, lower triangle) at the highest temperatures comprise di-borides and carbides (e.g., ZrB_2/ZrC, etc.). Note that, material combinations marked as stable will likely fail when one or more of the components of the bilayer structure undergo a phase transformation (i.e., melting or a displacive phase transition). When considering the bilayer emitter, the failure temperature may be lower than the melting point of either individual component due to possible eutectics or phase transitions.

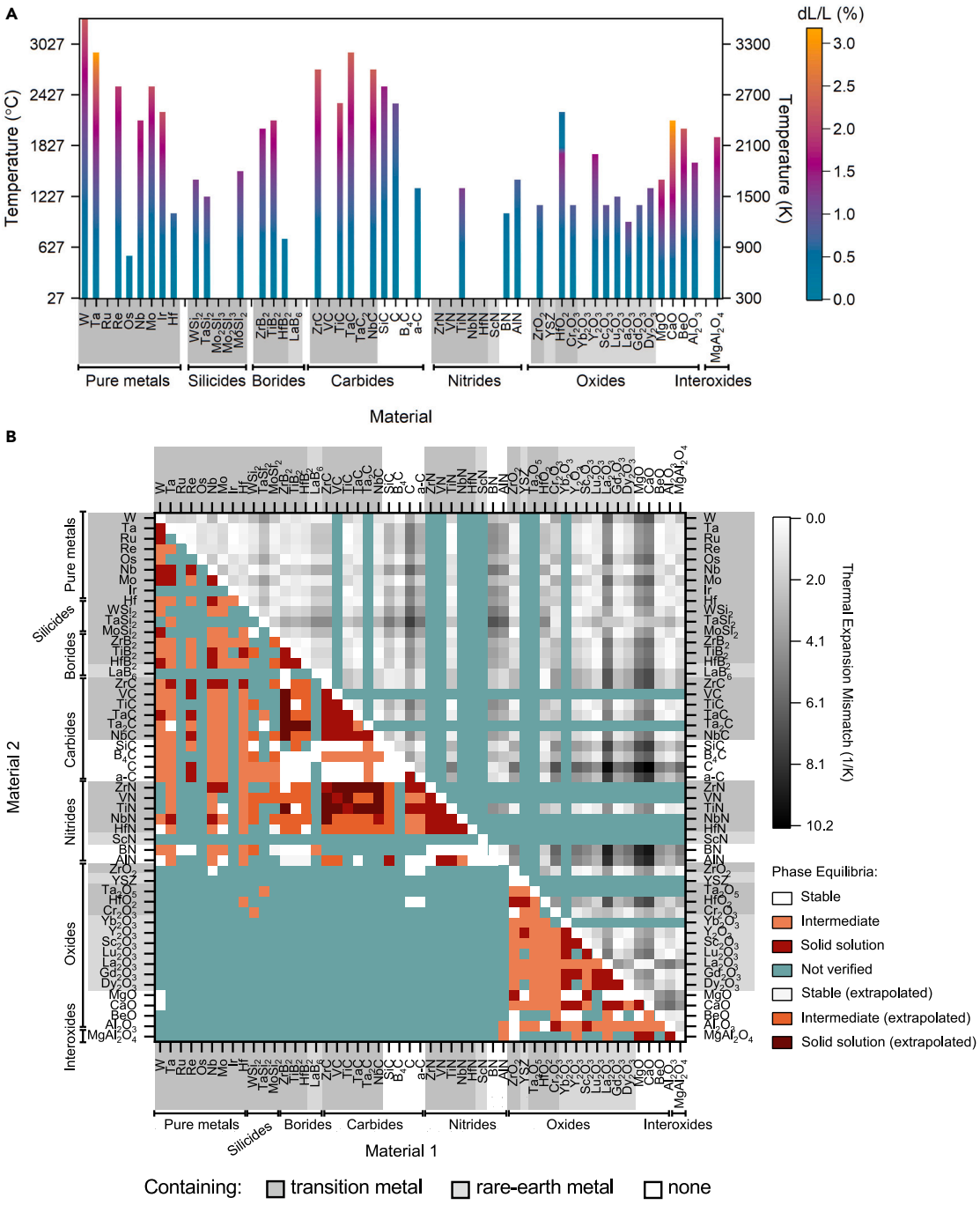

Figure 5. Thermal properties

(A) Linear thermal expansion as a function of temperature for materials with melting point >2,000°C (2,273.15 K). *dL/L* refers to the percent change in length, using 25°C (298.15 K) as the reference. Data from Touloukian[63] and Touloukian et al.[64]

(B) Thermal expansion mismatch (grayscale data, upper triangle) and phase equilibria (lower triangle) for selected materials (data calculated from FactSage[65] and the NIST Standard Reference Database 31, also known as the ACerS-NIST Phase Equilibria Database v4.9[66]). Extrapolated points are extracted from phase diagrams within ranges that are not validated. The teal points refer to data that are not verified.

Materials that have a driving force over the interface ($\nabla\mu \neq 0$) will change and can form a solid solution (red and maroon in Figure 5B, lower triangle) or intermediate compound (orange shades in Figure 5B, lower triangle). Examples of materials

forming a solid solution and an intermediate compound are ZrB_2/TiB_2 and ZrO_2/Ta_2O_5, respectively. In the former, Zr and Ti atoms can diffuse within the diborides hexagonal structure, forming a (Zr, Ti)B_2 solid solution. In the latter, the system reacts to form compounds such as $Zr_6Ta_2O_{17}$ with new structures and properties. These unstable systems are typically undesirable as the emitter properties could change during operation. However, they can have a lifetime, t, that depends on their kinetics. Here, t is proportional to the diffusion length (L) squared divided by the diffusion coefficient ($D(T)$) $\left(\text{i.e.,} t \propto \frac{L^2}{D(T)}\right)$, where $D(T) = D_0 e^{\frac{-Q}{RT}}$, with Q as the activation energy for diffusion in units of J/mol and R as the molar gas constant.[69] Therefore, diffusion can dramatically accelerate, increasing the likelihood of dissolution or reaction if $T > \left|\frac{-Q}{R}\right|$. Conversely, these thermochemically unstable material combinations might be kinetically stabilized at lower temperatures (~1,000°C), depending on their kinetics, allowing for photonic applications at these elevated temperatures.

Vapor pressure is another relevant thermochemical quantity when designing emitters for operation at high temperatures and/or in environments below ambient pressure, which can lead to material degradation. The lower the material's vapor pressure, the less likely the material is to sublimate when at high temperatures and vacuum-relevant pressures. Figure 6A is a summary of vapor pressures collected from the literature and calculated at 1,800°C for the coating materials considered in this work (see also Figures S15–S17). For single-element refractory metals, such as Ta, the total vapor pressure simply entails the contribution of the pure element[70] (i.e., the total pressure is the partial pressure of Ta). Alternatively, for compounds, evaporation or sublimation does not necessarily occur equally for their constituents. The total vapor pressure for a refractory oxide like MgO includes contributions from Mg, O_2, MgO, and other components[71] (i.e., the total pressure is the sum of the partial pressure of Mg, O_2, MgO, etc.). Despite the lack of information for some of the coating options, it is evident that refractory metals and selected oxides exhibit a vapor pressure of up to 2.7 $\times 10^{-3}$ Torr (3.6 $\times 10^{-6}$ atm) at 1,800°C, making them suited for many TPV experiments. Although the vapor pressures for AlN and BN are higher, 4.6 Torr (6.1 $\times 10^{-3}$ atm) and 0.22 Torr (2.9 $\times 10^{-4}$ atm), respectively, at 1,800°C, these nitride-based coatings can potentially tolerate temperatures up to 1,200°C when subjected to roughing pump vacuum regimes (10^{-3} Torr or 1.3 $\times 10^{-6}$ atm), as depicted in Figure 6B. Depending on the base pressure (vacuum level) in which the emitter will operate, a decrease in temperature might be necessary to avoid material sublimation/degradation. To overcome this obstacle with such materials, the emitter could instead operate at ambient gas pressure or increased gas pressure to reduce/eliminate sublimation. This result could be achieved by placing the high-temperature emitter in a separate enclosure or further away from the PV cell to suppress heat conduction and convection. In this scenario, focusing optics could be added, if needed, to assure light absorption by the PV cell.

Material selection for TPV emitters

When selecting the optimal emitter structures for a given TPV technology, we start with combinations that yield the highest FOM (Figures 4 and S10–S13) and downselect based on the ones that have thermal expansion mismatch <3.5% and are expected to be thermochemically stable (Figure 5). For structures that yield similar FOMs for a particular cell type, the emitter that results in the highest P_{cell} is chosen. Figure 7 and Table 1 show the emitter and cell spectral power density and the light J-V curves for optimized high-performance cell-emitter pairs for each PV cell type (see Tables S1–S5 for additional stable emitter options). We observe that these TPV pairs (InGaAsSb-BN/HfB_2, InGaAs-AlN/W, Ge-AlN/W, GaSb-AlN/W,

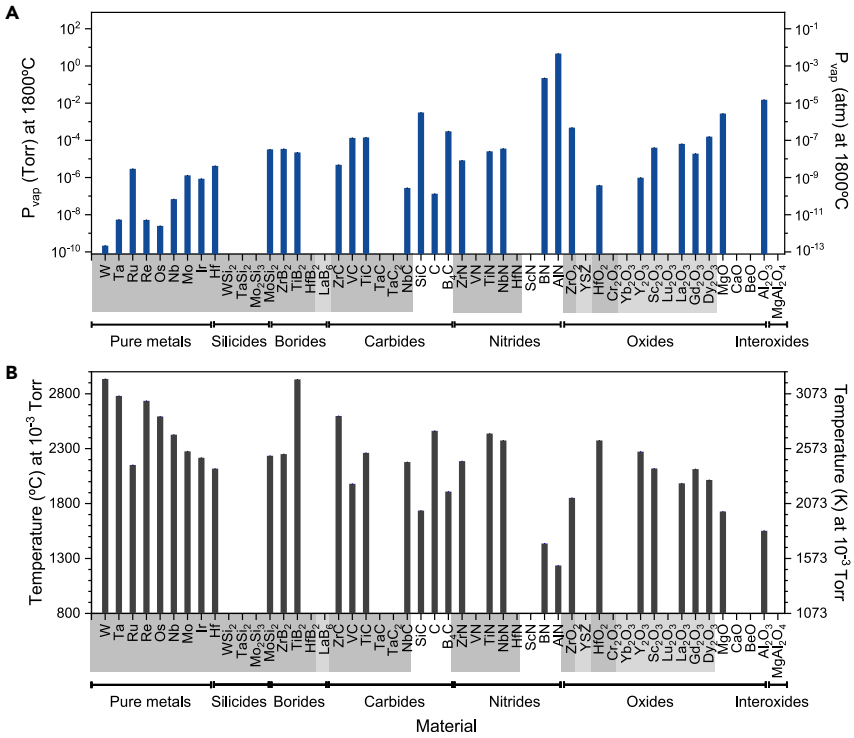

Figure 6. Vapor pressure

(A) Vapor pressure at 1,800°C.

(B) Temperature at which sublimation or evaporation occurs at 10^{-3} Torr for materials with melting point >2,000°C (2,273.15 K). Data from Edwards et al.,[70] Brewer and Porter,[71] Robson and Gilles,[72] Panish and Reif,[73] Kibler et al.,[74] Grimley et al.,[75] Fujishiro,[76] Dreger et al.,[77] Tripathy,[78] Hoch et al.,[79] Marshall and Norton,[80] Davis et al.,[81] Deadmore,[82] Gordienko et al.,[83] Verkhoglyadova and Sarsonov,[84] Kematick,[85] Hampson and Walker,[86] Vozzella et al.,[87] Speiser et al.,[88] Plante and Szwarc,[89] Carrera et al.,[90] Szwarc et al.,[91] Schulz et al.,[92] and Hoch et al.[93]

and Si-AlN/Mo) exhibit excellent spectral management, consistent with the concept that tuning of the broad spectrum of thermal emission is essential for high-performance systems. BN/HfB_2, AlN/W, and AlN/Mo have experimental data to validate their thermochemical stabilities. BN/HfB_2 has been observed to be stable *ex situ* experimentally up to 1,800°C when heated in Ar containing less than 0.1% N_2.[94] More experiments above 1,800°C are required to validate its upper-temperature stability. AlN/W and AlN/Mo have both been observed to be stable *ex situ* experimentally up to 1,700°C at $\sim 1 \times 10^{-7} - 1 \times 10^{-9}$ atm[95]; however, it was noted that AlN began to decompose and evaporate above 1,500°C at these vacuum pressures.

We also note that our approach allows matching the PV cell band gap to the emission spectrum of the emitter, maximizing the FOM given the emitter temperature (see Figures 7A and 7B). For generality, the cells used in our calculations have ideal IQE and antireflection coating, achieving 100% in-band absorption and carrier collection and 0% out-band absorption to focus on the emitter design rather than the cell fabrication. Leading TPVs do not have 100% in-band absorption and collection, but they do utilize back-surface reflectors to recuperate out-of-band photons, promoting an enhancement in spectral utilization and efficiency (FOM). For the analysis presented here, we have not incorporated back reflectors for the out-of-band photons, but they can easily be included within the formalism by modifying the

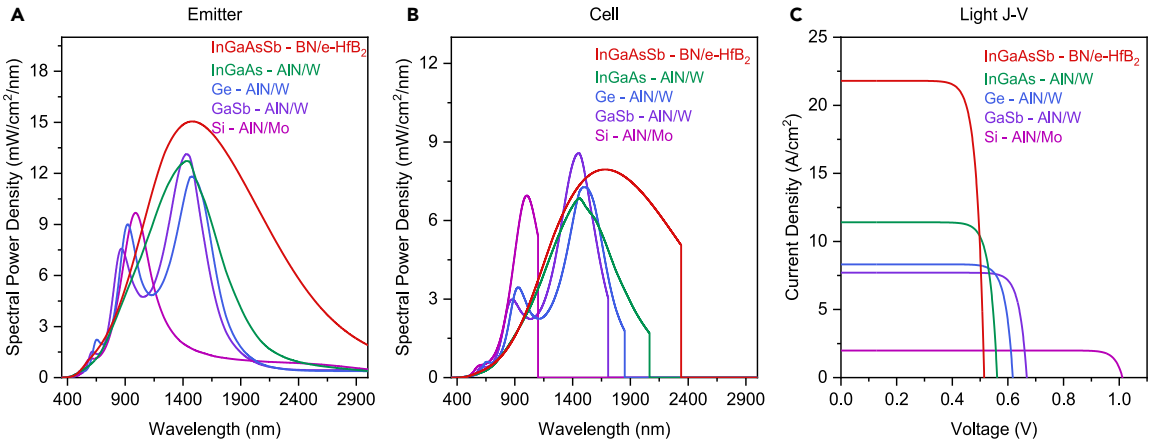

Figure 7. Highest-performing TPV systems

(A and B) Output power density as a function of wavelength for (A) optical emitter and (B) TPV cell. (C) Light *J-V* curve for top material combinations.

FOM to be $P_{cell}/(P_{emit} - P_{reabs})$, where P_{reabs} is the power from the emitter that is below the band gap of the PV cell. With the addition of an ideal back reflector for the out-of-band photons, P_{reabs} is reflected back to the emitter and then absorbed. Although this process does not increase P_{cell}, it does increase the FOM. For the GaSb TPV with an optimized emitter, the FOM can be increased from 49.4% to 56.6% with the addition of a back reflector (we note that the FOM could be further increased if the emitter structure were reoptimized for this configuration).

An additional challenge in operating real TPVs at very high temperatures is that the increase in FOM with temperature is mainly due to an increase in the J_{sc}, which can lead to a reduction in *FF* due to additional series resistance at very high current density as well as a reduction in IQE. These effects will eventually result in the cell becoming current-limited. In terms of cell performance, the highest-performing TPV systems exhibit an FF above 0.8, which in our case is not attributed to differences in illumination[13] but is rather due to the PV cells' high V_{oc} and J_{sc}, see Figure 7C. Differences in cell fabrication can affect its performance; however, we show that these PV technologies are very promising as highly efficient TPV, with FOM > 45% for InGaAsSb-, InGaAs-, Ge-, and GaSb-based system and >33% for the Si-based one, surpassing the state-of-the-art ones.[3,96–98] With a P_{cell} of 1.78 W cm^{-2}, the Si-based pair is characterized at J_{sc} = 1.99 A cm^{-2}, which is twice the current Si-TPV.[99]

As stated earlier, the combination of high temperature and low pressure often adopted in TPV (and the proximity between the emitter and the PV cell) can lead to the unwanted sublimation of some of the coating materials. Table 2 displays the best emitter options for TPV in vacuum (at 10^{-3} Torr). For the emitters containing B_4C operating at higher temperatures or lower pressures, B_4C sublimates, but the rate for B is higher than for C, resulting in a graphite phase at the top surface of the film.[72] Specifically, under 3.5 $\times 10^{-3}$ Torr (4.6×10^{-6} atm), B_4C sublimates at ~2,029°C, which is well above the temperature range considered in this perspective. In the case of MgO coatings, as stated earlier, different species can be formed in the vapor phase, leading to non-stochiometric sublimation.[71] Finally, Mo films are considered relatively stable at 10^{-3} Torr for 1,800°C, in the absence of oxygen.[87] Overall, the FOMs presented in Tables 1 and 2 are similar (note: BN(144 nm)/e-HfB_2 is selected for InGaAsSb in the inert environment [see Table 1] because it

Table 1. Thermophotovoltaic cell options and their respective most promising optical emitters (coating thickness in parentheses) for inert environment applications, considering both optical and thermal properties of materials

TPV cell	Band gap (eV)	Emitter coating (thickness)/substrate	FOM (%)	P_{emit} (W cm^{-2})	P_{cell} (W cm^{-2})	J_{sc} (A cm^{-2})	V_{oc} (V)	FF	J_m (A cm^{-2})	V_m (V)
InGaAsSb	0.53	BN(144 nm)/e-HfB_2	45.6	19.8	9.05	21.8	0.51	0.81	20.6	0.44
InGaAs	0.6	AlN(148 nm)/W	47.1	11.1	5.24	11.4	0.56	0.82	10.8	0.48
Ge	0.67	AlN(506 nm)/W	48.8	8.74	4.27	8.32	0.62	0.83	7.94	0.54
GaSb	0.73	AlN(473 nm)/W	49.4	8.75	4.32	7.70	0.67	0.84	7.38	0.59
Si[a]	1.1	AlN(315 nm)/Mo	33.3	5.34	1.78	1.99	1.01	0.88	1.93	0.92

All relevant parameters that quantify TPV performance are included for comparison.
[a]Si efficiencies >50% are possible with low output power densities (<0.3 W cm^{-2}).

can potentially deliver >19 W cm^{-2} with only a minor decrease in FOM compared with the selected emitter in vacuum, Table 2). Nonetheless, for all TPV cells, the values of FOM and P_{cell} are comparable, with performance considerably above reports from the literature, indicating that our material screening approach has identified emitter options that are worthy of exploring experimentally.

CONCLUSIONS AND OUTLOOK

In summary, we provided a pathway to achieve high-efficiency TPV performance by combining the optical and thermodynamic properties of 53 materials with melting points >2,000°C (2,273.15 K), spanning a wide range of PV cell materials (E_g range: 0.53–1.1 eV). Our results illustrate that design choices that have enhanced emitter-to-cell spectral matching, via thin films, can lead to a substantial gain in performance, enabling FOMs >45% for InGaAsSb-, InGaAs-, Ge-, and GaSb-based TPV system and 33% for practical Si cells. Our approach can overcome the challenge of thermal stability of the optical emitter, closing the performance gap between emitter and cell pairs by providing scaled-up, high-performance optical components. By learning from and integrating the best designs within the TPV metric, a significant gain in performance is within reach, bringing major opportunities for realizing ultra-high-temperature photonics systems for widespread impact applications.

The presented optimal structures of the TPV emitters are robust and demonstrate the viability of our optimization toward obtaining a highly selective TPV emitter with a scalable fabrication method. Our framework also demonstrates the possibility of designing metamaterials for specific applications in high-temperature photonics via optimization and machine learning, such as next-generation thermal emitters and barrier coatings. However, the expansion of our work would rely on the experimental data at ultra-high temperatures; thus, additional characterization methods are still required. In particular, *in situ* spectroscopic ellipsometry could be applied to obtain the refractive index of materials at ultra-high temperatures. Likewise, high-temperature calorimetry, dilatometry, and *in situ* X-ray diffraction techniques would be

Table 2. Thermophotovoltaic cell options and their respective most promising optical emitters, at 1,800°C, for application in vacuum (pressure ≤ 10^{-3} Torr), considering materials' vapor pressure, thermochemical stability, and optical properties

TPV cell	Band gap (eV)	Emitter coating (thickness)/substrate	FOM (%)	P_{emit} (W cm^{-2})	P_{cell} (W cm^{-2})	J_{sc} (A cm^{-2})	V_{oc} (V)	FF	J_m (A cm^{-2})	V_m (V)
InGaAsSb	0.53	B_4C(416 nm)/HfB_2	46.7	16.3	7.52	18.4	0.51	0.81	17.4	0.44
InGaAs	0.6	B_4C(351 nm)/HfB_2	45.6	15.4	7.04	15.08	0.57	0.82	14.3	0.49
Ge	0.67	MgO(166 nm)/W	47.3	9.91	4.68	9.90	0.62	0.83	8.67	0.54
GaSb	0.73	MgO(146 nm)/W	47.0	9.96	4.57	8.31	0.67	0.84	7.96	0.59
Si	1.1	Mo(26 nm)/TiN	30.2	3.07	0.93	1.06	1.00	0.88	1.03	0.90

All relevant parameters that quantify TPV performance are included for comparison.

necessary to expand our library of thermal expansion mismatch and phase equilibria between two materials. We anticipate that the implementation and development of ultra-high-temperature characterization methods would thus enable new thin-film emitters to be quickly screened for thermally stable and durable devices using this paradigm. We foresee this strategy enabling a pathway for TPV with >50% power conversion efficiency and applications to other high-temperature systems and thermal devices with improved functionality and stability.

SUPPLEMENTAL INFORMATION

Supplemental information can be found online at https://doi.org/10.1016/j.joule.2023.08.015.

ACKNOWLEDGMENTS

J.N.M., M.S.L., and S.J.M. thank the financial support from DARPA (award #HR00112190008). M.R.S.D. thanks the financial support from the University of Richmond, School of Arts and Science. Part of this study was carried out at the UC Davis Center for Nano and Micro Manufacturing (CNM2).

AUTHOR CONTRIBUTIONS

M.S.L. and J.N.M. conceived and managed the project. M.R.S.D. performed optical and detailed balance simulations and analysis. T.G. performed initial calculations of optical emitters. M.A.D. compiled and analyzed optical materials data. S.C.N. and S.J.M. performed thermochemical, stability, and vapor pressure analysis. M.R.S.D., S.J.M., M.S.L., and J.N.M. wrote the manuscript, and all authors contributed to its editing.

DECLARATION OF INTERESTS

The authors declare no competing interests.

REFERENCES

1. Green, M.A. (2003). Third Generation Photovoltaics: Advanced Solar Energy Conversion (Springer).

2. Tervo, E.J., France, R.M., Friedman, D.J., Arulanandam, M.K., King, R.R., Narayan, T.C., Luciano, C., Nizamian, D.P., Johnson, B.A., Young, A.R., et al. (2022). Efficient and scalable GaInAs thermophotovoltaic devices. Joule *6*, 2566–2584. https://doi.org/10.1016/j.joule.2022.10.002.

3. Fan, D., Burger, T., McSherry, S., Lee, B., Lenert, A., and Forrest, S.R. (2020). Near-perfect photon utilization in an air-bridge thermophotovoltaic cell. Nature *586*, 237–241. https://doi.org/10.1038/s41586-020-2717-7.

4. Omair, Z., Scranton, G., Pazos-Outón, L.M., Xiao, T.P., Steiner, M.A., Ganapati, V., Peterson, P.F., Holzrichter, J., Atwater, H., and Yablonovitch, E. (2019). Ultraefficient thermophotovoltaic power conversion by band-edge spectral filtering. Proc. Natl. Acad. Sci. USA *116*, 15356–15361. https://doi.org/10.1073/pnas.1903001116.

5. Narayan, T.C., Kuritzky, L.Y., Nizamian, D.P., Johnson, B.A., Tervo, E.J., Young, A.R., Luciano, C., Arulanandam, M.K., Kayes, B.M., Perl, E.E., et al. (2020). World record demonstration of > 30% thermophotovoltaic conversion efficiency. In 47th IEEE Photovoltaic Specialists Conference (PVSC), pp. 1792–1795. https://doi.org/10.1109/PVSC45281.2020.9300768.

6. LaPotin, A., Schulte, K.L., Steiner, M.A., Buznitsky, K., Kelsall, C.C., Friedman, D.J., Tervo, E.J., France, R.M., Young, M.R., Rohskopf, A., et al. (2022). Thermophotovoltaic efficiency of 40%. Nature *604*, 287–291. https://doi.org/10.1038/s41586-022-04473-y.

7. Bierman, D.M., Lenert, A., Chan, W.R., Bhatia, B., Celanović, I., Soljačić, M., and Wang, E.N. (2016). Enhanced photovoltaic energy conversion using thermally based spectral shaping. Nat. Energy *1*, 16068. https://doi.org/10.1038/nenergy.2016.68.

8. Lenert, A., Bierman, D.M., Nam, Y., Chan, W.R., Celanović, I., Soljačić, M., and Wang, E.N. (2014). A nanophotonic solar thermophotovoltaic device. Nat. Nanotechnol. *9*, 126–130. https://doi.org/10.1038/nnano.2013.286.

9. Suemitsu, M., Asano, T., Inoue, T., and Noda, S. (2020). High-efficiency thermophotovoltaic system that employs an emitter based on a silicon rod-type photonic crystal. ACS Photonics *7*, 80–87. https://doi.org/10.1021/acsphotonics.9b00984.

10. Chirumamilla, M., Krishnamurthy, G.V., Rout, S.S., Ritter, M., Störmer, M., Petrov, A.Y., and Eich, M. (2020). Thermal stability of tungsten based metamaterial emitter under medium vacuum and inert gas conditions. Sci. Rep. *10*, 3605. https://doi.org/10.1038/s41598-020-60419-2.

11. Chirumamilla, M., Krishnamurthy, G.V., Knopp, K., Krekeler, T., Graf, M., Jalas, D., Ritter, M., Störmer, M., Petrov, A.Y., and Eich, M. (2019). Metamaterial emitter for thermophotovoltaics stable up to 1400 °C. Sci. Rep. *9*, 7241. https://doi.org/10.1038/s41598-019-43640-6.

12. Woolf, D.N., Kadlec, E.A., Bethke, D., Grine, A.D., Nogan, J.J., Cederberg, J.G., Bruce Burckel, D., Luk, T.S., Shaner, E.A., and Hensley, J.M. (2018). High-efficiency thermophotovoltaic energy conversion enabled by a metamaterial selective emitter. Optica *5*, 213. https://doi.org/10.1364/OPTICA.5.000213.

13. Burger, T., Sempere, C., Roy-Layinde, B., and Lenert, A. (2020). Present efficiencies and future opportunities in thermophotovoltaics. Joule *4*, 1660–1680. https://doi.org/10.1016/j.joule.2020.06.021.

14. Sakakibara, R., Stelmakh, V., Chan, W.R., Ghebrebrhan, M., Joannopoulos, J.D., Soljačić, M., and Čelanović, I. (2019). Practical emitters

for thermophotovoltaics: a review. J. Photon. Energy *9*, 1. https://doi.org/10.1117/1.JPE.9.032713.

15. Hassan, S., Doiron, C.F., and Naik, G.V. (2020). Optimum selective emitters for efficient thermophotovoltaic conversion. Appl. Phys. Lett. *116*, 023903. https://doi.org/10.1063/1.5131367.

16. Kudyshev, Z.A., Kildishev, A.V., Shalaev, V.M., and Boltasseva, A. (2020). Machine-learning-assisted metasurface design for high-efficiency thermal emitter optimization. Appl. Phys. Rev. *7*, 021407. https://doi.org/10.1063/1.5134792.

17. Xu, Y., Gong, T., and Munday, J.N. (2015). The generalized Shockley-Queisser limit for nanostructured solar cells. Sci. Rep. *5*, 13536. https://doi.org/10.1038/srep13536.

18. Harder, N., and W rfel, P. (2003). Theoretical limits of thermophotovoltaic solar energy conversion. Semicond. Sci. Technol. *18*, S151–S157. https://doi.org/10.1088/0268-1242/18/5/303.

19. Yeng, Y.X., Chan, W.R., Rinnerbauer, V., Joannopoulos, J.D., Soljačić, M., and Celanovic, I. (2013). Performance analysis of experimentally viable photonic crystal enhanced thermophotovoltaic systems. Opt. Express *21*, A1035–A1051. https://doi.org/10.1364/OE.21.0A1035.

20. Yeng, Y.X., Chan, W.R., Rinnerbauer, V., Stelmakh, V., Senkevich, J.J., Joannopoulos, J.D., Soljacic, M., and Čelanović, I. (2015). Photonic crystal enhanced silicon cell based thermophotovoltaic systems. Opt. Express *23*, A157–A168. https://doi.org/10.1364/OE.23.00A157.

21. Chirumamilla, M., Roberts, A.S., Ding, F., Wang, D., Kristensen, P.K., Bozhevolnyi, S.I., and Pedersen, K. (2016). Multilayer tungsten-alumina-based broadband light absorbers for high-temperature applications. Opt. Mater. Express *6*, 2704–2714. https://doi.org/10.1364/OME.6.002704.

22. Silva-Oelker, G., Jerez-Hanckes, C., and Fay, P. (2019). High-temperature tungsten-hafnia optimized selective thermal emitters for thermophotovoltaic applications. J. Quant. Spectrosc. Radiat. Transf. *231*, 61–68. https://doi.org/10.1016/j.jqsrt.2019.04.008.

23. Yang, Z.-Y., Ishii, S., Doan, A.T., Shinde, S.L., Dao, T.D., Lo, Y.-P., Chen, K.-P., and Nagao, T. (2020). Narrow-band thermal emitter with titanium nitride thin film demonstrating high temperature stability. Adv. Opt. Mater. *8*, 1900982. https://doi.org/10.1002/adom.201900982.

24. E.D. Palik, ed. (1991). Handbook of Optical Constants of Solids (Academic Press).

25. Antonov, V.N., Antonov, V.N., Jepsen, O., Andersen, O.K., Borghesi, A., Bosio, C., Marabelli, F., Piaggi, A., Guizzetti, G., and Nava, F. (1991). Optical Properties of WSi_(2). Phys. Rev. B: Condens. Matter *44*, 8437–8445.

26. Tanaka, M., Kurita, S., Fujisawa, M., and Levy, F. (1992). Optical properties of single-crystal TaSi_(2) in the photon-energy range 0.6–20 eV. Phys. Rev. B Condens. Matter *46*, 10442–10445.

27. Hernández-Pinilla, D., Rodríguez-Palomo, A., Álvarez-Fraga, L., Céspedes, E., Prieto, J.E., Muñoz-Martín, A., and Prieto, C. (2016). $MoSi_2$–Si_3N_4 absorber for high temperature solar selective coating. Sol. Energy Mater. Sol. Cells *152*, 141–146.

28. Hoat, D.M. (2019). Electronic structure, chemical bonding, optical, elastic and dynamical properties of MeB2 compounds: effect of transition metal Me = Sc, Ti and Zr. Comp. Condens. Matter *21*, e00406. https://doi.org/10.1016/j.cocom.2019.e00406.

29. Yang, Y., Jayaraman, S., Sperling, B., Kim, D.Y., Girolami, G.S., and Abelson, J.R. (2007). In situ spectroscopic ellipsometry analyses of hafnium diboride thin films deposited by single-source chemical vapor deposition. Journal of Vacuum Science and Technology A *25*, 200–206.

30. van der Heide, P.A.M., ten Cate, H.W., ten Dam, L.M., de Groot, R.A., and de Vroomen, A.R. (1986). Differences between LaB6and CeB6by means of spectroscopic ellipsometry. J. Phys. F *16*, 1617–1623. https://doi.org/10.1088/0305-4608/16/10/026.

31. Modine, F.A., Haywood, T.W., and Allison, C.Y. (1985). Optical and electrical properties of single-crystalline zirconium carbide. Phys. Rev. B Condens. Matter *32*, 7743–7747.

32. Modine, F.A., Major, R.W., Haywood, T.W., Gruzalski, G.R., and Smith, D.Y. (1984). Optical properties of tantalum carbide from the infrared to the near ultraviolet. Phys. Rev. B *29*, 836–841. https://doi.org/10.1103/PhysRevB.29.836.

33. Jubair, M., Karim, A.T., Nuruzzaman, M., and Zilani, M.A.K. (2019). Comparison of structural, mechanical and optical properties of tantalum hemicarbide with tantalum monocarbide: ab initio calculations. J. Phys. Commun. *3*, 055017.

34. Koide, T., Shidara, T., Fukutani, H., Fujimori, A., Miyahara, T., Kato, H., Otani, S., and Ishizawa, Y. (1990). Optical study of the stoichiometry-dependent electronic structure of TiC_{x}, VC_{x}, and NbC_{x}. Phys. Rev. *42*, 4979.

35. Larruquert, J.I., Pérez-Marín, A.P., García-Cortés, S., Rodríguez-de Marcos, L., Aznárez, J.A., and Méndez, J.A. (2011). Self-consistent optical constants of SiC thin films. J. Opt. Soc. Am. A Opt. Image Sci. Vis. *28*, 2340–2345. https://doi.org/10.1364/JOSAA.28.002340.

36. Larruquert, J.I., Pérez-Marín, A.P., García-Cortés, S., Rodríguez-de Marcos, L., Aznárez, J.A., and Méndez, J.A. (2012). Self-consistent optical constants of sputter-deposited B4C thin films. J. Opt. Soc. Am. A Opt. Image Sci. Vis. *29*, 117–123. https://doi.org/10.1364/JOSAA.29.000117.

37. Guo, W.-P., Mishra, R., Cheng, C.-W., Wu, B.-H., Chen, L.-J., Lin, M.-T., and Gwo, S. (2019). Titanium nitride epitaxial films as a plasmonic material platform: alternative to gold. ACS Photonics *6*, 1848–1854. https://doi.org/10.1021/acsphotonics.9b00617.

38. Banerjee, A., Heath, R.M., Morozov, D., Hemakumara, D., Nasti, U., Thayne, I., and Hadfield, R.H. (2018). Optical properties of refractory metal based thin films. Opt. Mater. Express *8*, 2072. https://doi.org/10.1364/OME.8.002072.

39. Saha, B., Naik, G., Drachev, V.P., Boltasseva, A., Marinero, E.E., and Sands, T.D. (2013). Electronic and optical properties of ScN and (Sc,Mn)N thin films deposited by reactive DC-magnetron sputtering. J. Appl. Phys. *114*, 063519.

40. Adachi, S. (1999). Optical Constants of Crystalline and Amorphous Semiconductors (Springer). https://doi.org/10.1007/978-1-4615-5247-5.

41. Pastrňák, J., and Roskovcová, L. (1966). Refraction index measurements on AlN single crystals. Phys. Status Solidi B *14*, K5–K8. https://doi.org/10.1002/pssb.19660140127.

42. Synowicki, R.A., and Tiwald, T.E. (2004). Optical properties of bulk c-ZrO2, c-MgO and a-As2S3 determined by variable angle spectroscopic ellipsometry. Thin Solid Films *455–456*, 248–255. https://doi.org/10.1016/j.tsf.2004.02.028.

43. Al-Kuhaili, M.F. (2004). Optical properties of hafnium oxide thin films and their application in energy-efficient windows. Opt. Mater. *27*, 383–387. https://doi.org/10.1016/j.optmat.2004.04.014.

44. Medenbach, O., Dettmar, D., Shannon, R.D., Fischer, R.X., and Yen, W.M. (2001). Refractive index and optical dispersion of rare earth oxides using a small-prism technique. J. Opt. A *3*, 174–177. https://doi.org/10.1088/1464-4258/3/3/303.

45. Wang, X., Liu, H., Zhao, L., Fei, C., Feng, X., Chen, S., and Wang, Y. (2017). Structural properties characterized by the film thickness and annealing temperature for La2O3 films grown by atomic layer deposition. Nanoscale Res. Lett. *12*, 233. https://doi.org/10.1186/s11671-017-2018-8.

46. Liu, C.J., and Sieckmann, E.F. (1966). Refractive index of calcium oxide. J. Appl. Phys. *37*, 2450–2452. https://doi.org/10.1063/1.1708835.

47. Lichtenstein, T.; University of Rochester; College of Engineering and Applied Science (1979). Handbook of Thin Film Materials (College of Engineering and Applied Science, University of Rochester).

48. Belosludtsev, A., Juškevičius, K., Ceizaris, L., Samuilovas, R., Stanionytė, S., Jasulaitienė, V., and Kičas, S. (2018). Correlation between stoichiometry and properties of scandium oxide films prepared by reactive magnetron sputtering. Appl. Surf. Sci. *427*, 312–318. https://doi.org/10.1016/j.apsusc.2017.08.068.

49. Guler, U., Boltasseva, A., and Shalaev, V.M. (2014). Applied physics. Refractory plasmonics. Science *344*, 263–264. https://doi.org/10.1126/science.1252722.

50. Zhou, Z., Chen, Q., and Bermel, P. (2015). Prospects for high-performance thermophotovoltaic conversion efficiencies exceeding the Shockley–Queisser limit. Energy Convers. Manag. *97*, 63–69. https://doi.org/10.1016/j.enconman.2015.03.035.

51. Sai, H. (2004). Thermophotovoltaic generation with microstructured tungsten selective emitters. In AIP Conf. Proc. (AIP), pp. 206–214. https://doi.org/10.1063/1.1841896.

52. Herve, P., and Sadou, A. (2008). Determination of the complex index of refractory metals at

high temperatures: application to the determination of thermo-optical properties. Infrared Phys. Technol. *51*, 249–255. https://doi.org/10.1016/j.infrared.2007.07.002.

53. Briggs, J.A., Naik, G.V., Zhao, Y., Petach, T.A., Sahasrabuddhe, K., Goldhaber-Gordon, D., Melosh, N.A., and Dionne, J.A. (2017). Temperature-dependent optical properties of titanium nitride. Appl. Phys. Lett. *110*, 101901. https://doi.org/10.1063/1.4977840.

54. Reddy, H., Guler, U., Kudyshev, Z., Kildishev, A.V., Shalaev, V.M., and Boltasseva, A. (2017). Temperature-dependent optical properties of plasmonic titanium nitride thin films. ACS Photonics *4*, 1413–1420. https://doi.org/10.1021/acsphotonics.7b00127.

55. Florio, J.V. (1960). Dielectric properties of alumina at high temperatures. J. Am. Ceram. Soc. *43*, 262–267. https://doi.org/10.1111/j.1151-2916.1960.tb14594.x.

56. Belous, Ovchar, and Mischuk. (2003). Temperature trends of the permittivity in complex oxides of rare-earth elements with perovskite-type structure. Condens. Matter Phys. *6*, 251. https://doi.org/10.5488/CMP.6.2.251.

57. Bermel, P., Ghebrebrhan, M., Chan, W., Yeng, Y.X., Araghchini, M., Hamam, R., Marton, C.H., Jensen, K.F., Soljačić, M., Joannopoulos, J.D., et al. (2010). Design and global optimization of high-efficiency thermophotovoltaic systems. Opt. Express *18*, A314–A334. https://doi.org/10.1364/OE.18.00A314.

58. Almora, O., Cabrera, C.I., Garcia-Cerrillo, J., Kirchartz, T., Rau, U., and Brabec, C.J. (2021). Quantifying the Absorption Onset in the Quantum Efficiency of Emerging Photovoltaic Devices. Adv. Energy Mater. *11*, 2100022. https://doi.org/10.1002/aenm.202100022.

59. Rau, U. (2007). Reciprocity relation between photovoltaic quantum efficiency and electroluminescent emission of solar cells. Phys. Rev. B *76*, 085303. https://doi.org/10.1103/PhysRevB.76.085303.

60. Dias, M.R.S., Gong, C., Benson, Z.A., and Leite, M.S. (2018). Metal alloys for superabsorption: lithography-free, omnidirectional, CMOS-compatible AlCu alloys for thin-film superabsorbers (advanced optical materials 2/2018). Adv. Opt. Mater. *6*, 1870007. https://doi.org/10.1002/adom.201870007.

61. Lumb, M.P., Mack, S., Schmieder, K.J., González, M., Bennett, M.F., Scheiman, D., Meitl, M., Fisher, B., Burroughs, S., Lee, K.-T., et al. (2017). GaSb-based solar cells for full solar spectrum energy harvesting. Adv. En. Mater. *7*, 1700345. https://doi.org/10.1002/aenm.201700345.

62. Ferguson, L.G., and Fraas, L.M. (1995). Theoretical study of GaSb PV cells efficiency as a function of temperature. Sol. Energy Mater. Sol. Cells *39*, 11–18. https://doi.org/10.1016/0927-0248(95)00030-5.

63. Touloukian, Y.S. (1975). Thermal Expansion: Metallic Elements and Alloys (Springer).

64. Touloukian, Y.S., Kirby, R.K., Taylor, R.E., and Lee, T.Y.R. (1977). Thermal Expansion Nonmetallic Solids (Plenum Press).

65. Bale, C.W., Bélisle, E., Chartrand, P., Decterov, S.A., Eriksson, G., Gheribi, A.E., Hack, K., Jung, I.-H., Kang, Y.-B., Melançon, J., et al. (2016). FactSage thermochemical software and databases, 2010–2016. Calphad *54*, 35–53. https://doi.org/10.1016/j.calphad.2016.05.002.

66. Phase Equilibria Diagrams Database (NIST Standard Reference Database 31). (2022).

67. Xia, Z.C., and Hutchinson, J.W. (2000). Crack patterns in thin films. J. Mech. Phys. Solids *48*, 1107–1131. https://doi.org/10.1016/S0022-5096(99)00081-2.

68. Begley, M.R., and Hutchinson, J.W. (2017). The Mechanics and Reliability of Films, Multilayers and Coatings (Cambridge University Press). https://doi.org/10.1017/9781316443606.

69. O'Hayre, R.P. (2015). Materials Kinetics Fundamentals: Principles, Processes, and Applications (Wiley).

70. Edwards, J.W., Johnston, H.L., and Blackburn, P.E. (1951). Vapor pressure of inorganic substances. IV. Tantalum between 2624 and 2943°K. 1. J. Am. Chem. Soc. *73*, 172–174. https://doi.org/10.1021/ja01145a060.

71. Brewer, L., and Porter, R.F. (1954). A thermodynamic and spectroscopic study of gaseous magnesium oxide. J. Chem. Phys. *22*, 1867–1877. https://doi.org/10.1063/1.1739934.

72. Robson, H.E., and Gilles, P.W. (1964). The high temperature vaporization properties of boron carbide and the heat of sublimation of boron 1. J. Phys. Chem. *68*, 983–989.

73. Panish, M.B., and Reif, L. (1963). Thermodynamics of the vaporization of Hf and HfO_2: dissociation energy of HfO. J. Chem. Phys. *38*, 253–256. https://doi.org/10.1063/1.1733473.

74. Kibler, G., Lyon, T., Linevsky, M., and DeSantis, V. (1964). Carbonization of Plastics and Refractory Material Research (AF Materials Laboratory Research and Technology Division, Writgh-Parrerson Air Force Base).

75. Grimley, R.T., Burns, R.P., and Inghram, M.G. (1961). Thermodynamics of the vaporization of Cr_2O_3: dissociation energies of CrO, CrO_2, and CrO_3. J. Chem. Phys. *34*, 664–667. https://doi.org/10.1063/1.1701005.

76. Fujishiro, S. (1961). The dissociation pressure of VC at high temperature and the thermodynamic properties. Trans. Japan Inst. Met. *1*, 125–129.

77. Dreger, L.H., Dadape, V.V., and Margrave, J.L. (1962). Sublimation and decomposition studies on boron nitride and aluminum nitride 1. J. Phys. Chem. *66*, 1556–1559. https://doi.org/10.1021/j100814a515.

78. Tripathy, P.K. (2001). On the thermal decomposition of vanadium nitride. J. Mater. Chem. *11*, 1514–1518. https://doi.org/10.1039/b007792p.

79. Hoch, M., Dingledy, D.P., and Johnston, H.L. (1955). The vaporization of TiN and ZrN 1. J. Am. Chem. Soc. *77*, 304–306. https://doi.org/10.1021/ja01607a015.

80. Marshall, A.L., and Norton, F.J. (1950). Carbon vapor pressure and heat of vaporization. J. Am. Chem. Soc. *72*, 2166–2171. https://doi.org/10.1021/ja01161a081.

81. Davis, S.G., Anthrop, D.F., and Searcy, A.W. (1960). Vapor pressure of silicon and the dissociation pressure of silicon carbide. J. Chem. Phys. *34*, 659–664.

82. Deadmore, D.L. (1966). 1361. Vaporization of tantalum carbide-hafnium carbide solid solutions at 2500 to 3000°K. Vacuum *16*, 460. https://doi.org/10.1016/0042-207X(66)91629-0.

83. Gordienko, S.P., Samsonov, G.V., and Fesenko, V.V. (1965). The evaporation of lanthanum hexaboride. Powder Metall. Met. Ceram. *4*, 661–663. https://doi.org/10.1007/BF00774653.

84. Verkhoglyadova, T.S., and Sarsonov, G.V. (1985). Vapor pressure and evaporation rate of certain heat-resistant compounds in a vacuum at high temperatures. NASA-TM-77807. https://ntrs.nasa.gov/citations/19850010726.

85. Kematick, R.J. (1993). Vaporization thermodynamics of the tungsten silicides. J. Alloys Compd. *202*, 225–229. https://doi.org/10.1016/0925-8388(93)90543-V.

86. Hampson, R.F., and Walker, R.F. (1961). Vapor pressures of platinum, iridium, and rhodium. J. Res. Natl. Bur. Stand. A Phys. Chem. *65A*, 289–295. https://doi.org/10.6028/jres.065A.034.

87. Vozzella, P.A., Miller, A.D., and DeCrescente, M.A. (1964). Vapor pressure of molybdenum. J. Chem. Phys. *41*, 589–590. https://doi.org/10.1063/1.1725929.

88. Speiser, R., Blackburn, P., and Johnston, H.L. (1959). Vapor pressure of niobium. J. Electrochem. Soc. *106*, 52. https://doi.org/10.1149/1.2427264.

89. Plante, E.R., and Szwarc, R. (1966). Vapor pressure and heat of sublimation of rhenium. J. Res. Natl. Bur. Stand. A Phys. Chem. *70A*, 175–179. https://doi.org/10.6028/jres.070A.014.

90. Carrera, N.J., Walker, R.F., and Plante, E.R. (1964). Vapor pressures of ruthenium and osmium. J. Res. Natl. Bur. Stand. A Phys. Chem. *68A*, 325–330. https://doi.org/10.6028/jres.068A.031.

91. Szwarc, R., Plante, E.R., and Diamond, J.J. (1965). Vapor pressure and heat of sublimation of tungsten. J. Res. Natl. Bur. Stand. A Phys. Chem. *69A*, 417–421.

92. Schulz, U., Saruhan, B., Fritscher, K., and Leyens, C. (2005). Review on advanced EB-PVD ceramic topcoats for TBC applications. Int. J. Appl. Ceram. Technol. *1*, 302–315. https://doi.org/10.1111/j.1744-7402.2004.tb00182.x.

93. Hoch, M., Nakata, M., and Johnston, H.L. (1953). Vapor Pressures of Inorganic

Substances, Zirconium Dioxide (The Ohio State University).

94. Rudy, E., and Benesovsky, F. (1961). Untersuchungen in den systemen: Hafnium—Bor—Stickstof und zirkonium—Bor—Stickstoff. Monatsh. Chem. Verw. Teile Anderer Wiss. *92*, 415–441. https://doi.org/10.1007/BF01153900.

95. Borisova, A.L., and Martsenyuk, I.S. (1975). Reactions of boron and aluminum nitrides, and materials based on them, with refractory metals. Sov. Powder Metall. Met. Ceram. *14*, 822–826. https://doi.org/10.1007/BF00790818.

96. Dashiell, M.W., Beausang, J.F., Ehsani, H., Nichols, G.J., Depoy, D.M., Danielson, L.R., Talamo, P., Rahner, K.D., Brown, E.J., Burger, S.R., et al. (2006). Quaternary InGaAsSb Thermophotovoltaic Diodes. IEEE Trans. Electron Devices *53*, 2879–2891. https://doi.org/10.1109/TED.2006.885087.

97. Fernández, J., Dimroth, F., Oliva, E., Hermle, M., and Bett, A.W. (2007). Back-surface optimization of germanium TPV cells. In AIP Conf. Proc. (AIP), pp. 190–197. https://doi.org/10.1063/1.2711736.

98. Fraas, L.M., Samaras, J.E., Huang, H.X., Minkin, L.M., Avery, J.E., Daniels, W.E., and Hui, S. (2001). TPV generators using the radiant tube burner configuration. In Proceedings of 17th European PV Solar Energy Conference.

99. Lee, B., Lentz, R., Burger, T., Roy-Layinde, B., Lim, J., Zhu, R.M., Fan, D., Lenert, A., and Forrest, S.R. (2022). Air-bridge Si thermophotovoltaic cell with high photon utilization. ACS Energy Lett. *7*, 2388–2392. https://doi.org/10.1021/acsenergylett.2c01075.